Supporting Information

Plasmon-induced Charge Separation and Accumulation in $Ag_2S/Cu_{2-x}S$ S-Scheme Junction for Wide-Light-Driven Photothermal-Assisted Photocatalysis

Wen-Xi Xia [a], *Yi-Xin Dong* [a], *Zhe-Yuan Chen* [a], *Hai-Ting Li* [a], *You-Long Chen* [b], *Qing-Bo Liu* [a], *Si-Jing Ding* [c], *Qu-Quan Wang* *[d, e], *Liang Ma* [a] *

[a] Hubei Key Laboratory of Optical Information and Pattern Recognition, Wuhan Institute of Technology, Wuhan, 430205, P. R. China.

[b] State Key Laboratory of Pulsed Power Laser Technology, National University of Defense Technology, Hefei 230037, P. R. China.

[c] School of Mathematics and Physics, China University of Geosciences (Wuhan), Wuhan, 430074, P. R. China.

[d] Guangdong Provincial Key Laboratory of Advanced Thermoelectric Materials and Device Physics, Southern University of Science and Technology, Shenzhen, 518055, P. R. China.

[e] Quantum Science Center of Guangdong–Hong Kong–Macao Greater Bay Area (Guangdong), Shenzhen 518045, China

Experimental Section

1. Photocatalytic measurements

The photocatalytic hydrogen production measurement was conducted in a commercial test system (Labsolar-6A, Beijing Perfect Light). Typically, 20 mg of photocatalyst and 50 mL of sacrificial reagent Na_2S (0.35 M) and Na_2SO_3 (0.25 M) aqueous solution were added to a quartz reactor. The light source was a 300 W Xenon lamp equipped with a filter (> 420 nm). In the photocatalytic measurements, hydrogen was collected and detected by an on-line GC-9790 gas chromatograph equipped with a thermal conductivity detector, which Argon was used as the carrier gas. The apparent quantum efficiency (AQE) was tested with different irradiation light by using various quartz bandpass filters. A Ray virtual radiation actinometer was used to record the luminous flux of incident light.

2. Photoelectrochemical measurements

Photoelectrochemical measurements were used by CHI660 electrochemical workstation with a three-electrode cell. The photoanodes were made by coating photocatalysts on a FTO glass. Particularly, 20 mg of catalyst powder and 20 mg polyethylene glycol were added into 2 mL of ethanol to form a slurry. Then, the slurry was coated on a 2 cm × 1 cm FTO glass via a scraping coating method, which the active area of the electrode was kept as 1 cm × 1 cm. The coated electrode was dried at 200 °C in argon flow for 0.5 h. In the photoelectrochemical tests, the 1 cm × 1 cm Pt electrode was used counter electrode, and an Ag/AgCl electrode was used as the reference electrode. 0.5 M Na_2SO_4 aqueous solution was used as the electrolyte, and 300 W Xenon lamp was served as the simulated solar energy source. Electrochemical impedance spectroscopy (EIS) was acquired in dark under alternative current voltage (10 mV). It was tested with a direct current bias of 0.6 V against Ag/AgCl with a frequency range of 10^{-1} to 10^5 Hz.

3. Photothermal measurement

The photothermal measurement of as-prepared powder were carried out as follows, 40 mg of sample was loaded on a white paper and initial temperature was controlled at room temperature (27 °C). A 300 W Xenon lamp (100 mW/cm^2) was used as a light source. The temperature of the sample was measured using the infrared (IR) thermal camera. The photothermal measurements of as-prepared aqueous samples were carried out in the cuvette, and the temperature of sample was measured using the IR thermal camera and thermocouple. To evaluate the photothermal conversion of $Ag_2S/Cu_{2-x}S$, the aqueous solution (1.3 mL, 100 μg/mL) was irradiated by an 808 nm laser (1.0 W/cm^2). The temperature variation of the different samples was continuously monitored by an infrared (IR) thermal camera and thermocouple. The photothermal conversion efficiency (PCE) was calculated by the formula:

$$\eta = \frac{hs(T_{\max} - T_{surr}) - Q_{dis}}{I(1-10^{-A_\lambda})} \quad (1)$$

where *h* and *s* are the heat transfer coefficient and surface area of the container. $T_{\max}$, T_{surr}, and Q_{dis} are the maximum steady-state temperature, temperature of the surroundings, heat generated by the water and quartz cell under laser irradiation, respectively. I and A_λ are the incident laser intensity and absorbance at excitation wavelength, respectively.

Moreover, formula (2) was used.

$$hs = \frac{m_{H_2O}C_{H_2O}}{\tau_S} \quad (2)$$

where m_{H_2O} are the total mass of H_2O, C_{H_2O} denotes the specific heat capacity of H_2O, and τ_s is the time constant of $Ag_2S/Cu_{2-x}S$.

Then, formula (3) was used for the cooling period (i.e., after removing the 808 nm light source).

$$t = -\tau_s \times \ln\theta = -\ln\frac{T - T_{surr}}{T_{\max} - T_{surr}} \qquad (3)$$

where $T_{\max}$ is the highest steady-state temperature of $Ag_2S/Cu_{2-x}S$, T_{surr} is the ambient temperature, T represents the real-time temperature. Thus, the time constant quantity was calculated from the linear regression curve in cooling period of $Ag_2S/Cu_{2-x}S$.

4. TAS measurements

TAS measurements were performed on a pump-probe system (Femto-TA100), and all experiments were performed at ~24 °C. The aqueous solution samples (1 mg/mL), including Ag_2S, $Cu_{2-x}S$, and $Ag_2S/Cu_{2-x}S$ were deposited on quartz glasses (1 x 1 cm) and dried at 70 °C for further tests. The fundamental pulses were produced by a Ti: sapphire laser from Coherent (Astrella, 800 nm, 35 fs, 7 mJ/pulse, and 1 kHz repetition). The fundamental beam was focused into a CaF_2 or YAG crystal to produce a white light continuum probe beam with a time window limit of 3 ns. A fraction of the fundamental beam was utilized to generate the 400 nm pump beam through the optical parametric amplifier.

5. Sample Characterization

Transmission electron microscopy (TEM) and high-resolution TEM (HRTEM) measurements were performed on Talos F200S instruments. Scanning electron microscopy (SEM) characterization was performed on GeminiSEM 300. X-ray photoelectron spectroscopy (XPS) measurement was performed on Thermo Scientific ESCALAB Xi+ system. X-ray diffraction (XRD) was measured by a Bruker D8 ADVANCE X-ray diffractometer with Cu Kα radiation. UV-Vis-NIR absorption spectra were recorded on spectrophotometer (lambda 1050). *In-situ* surface potential images were conducted at an atomic force microscopy (Bruker Dimension Icon, German) operating in KPFM mode.

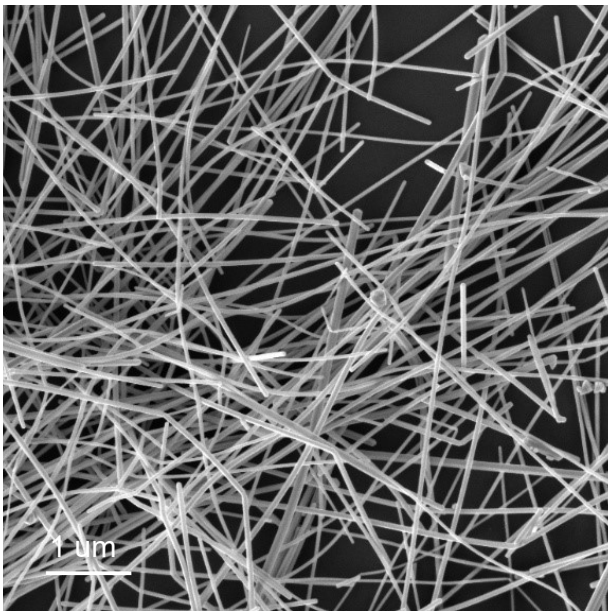

Figure S1. Low-magnification SEM image of Ag nanowires.

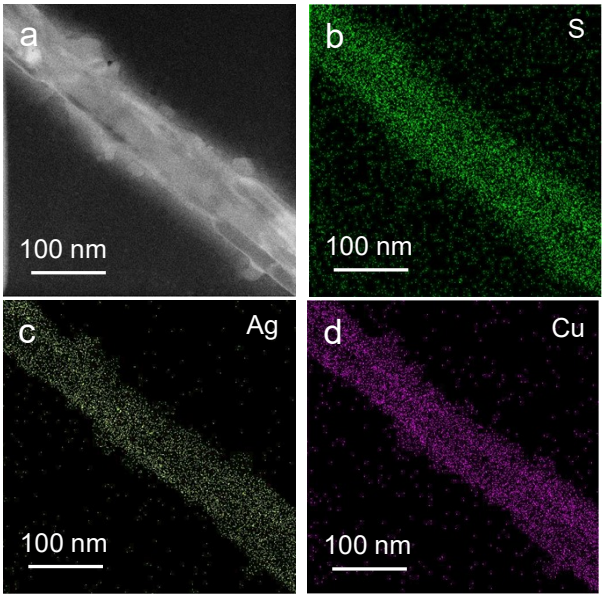

Figure S2. High-angle annular dark-field scanning TEM (HAADF-STEM) and energy-dispersive X-ray spectroscopy (EDS) mappings of $Ag_2S/Cu_{2-x}S$ heterostructures.

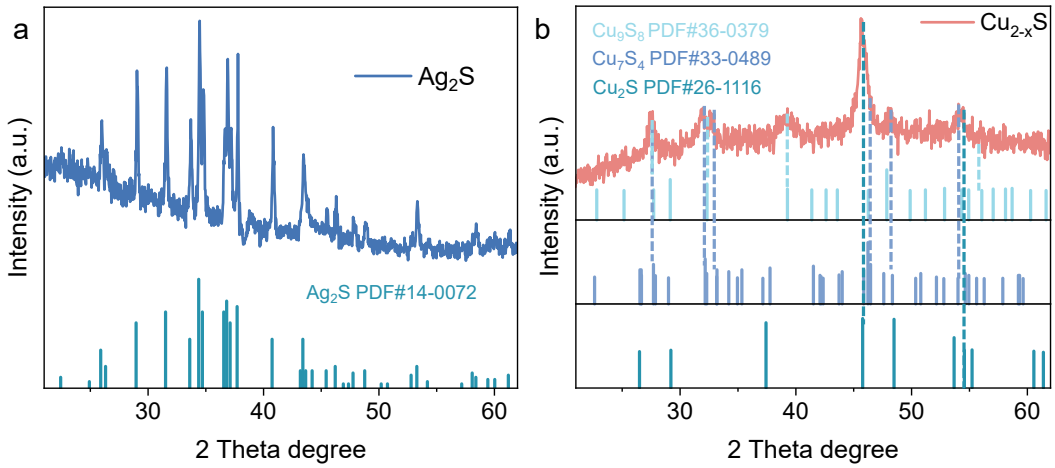

Figure S3. XRD patterns of the Ag_2S (a) and $Cu_{2-x}S$ (b).

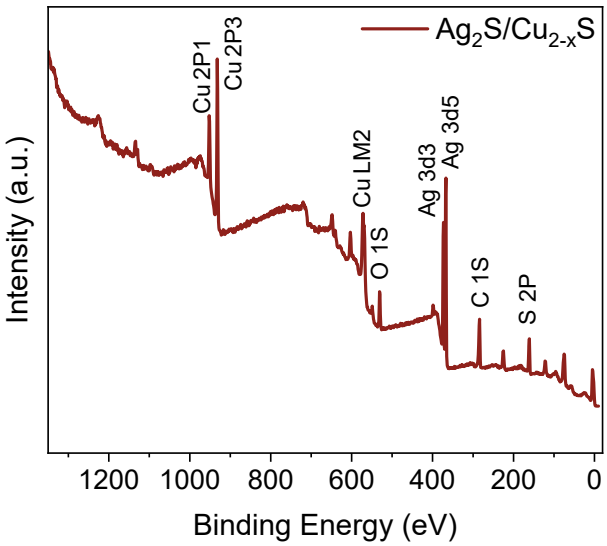

Figure S4. XPS survey of $Ag_2S/Cu_{2-x}S$ nanotubes.

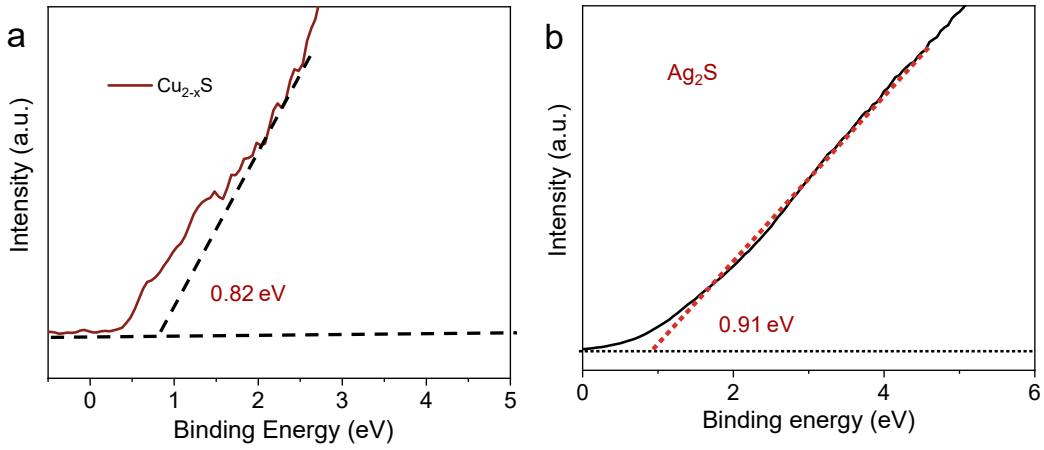

Figure S5. Valence band with respect to the Fermi level for $Cu_{2-x}S$ (a) and Ag_2S (b).

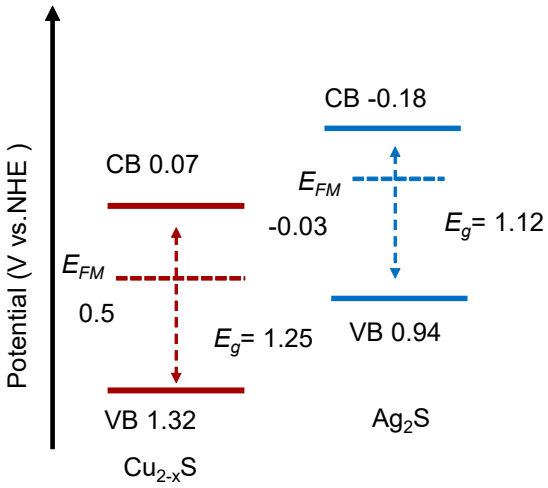

Figure S6. Calculated band structures for Ag_2S and $Cu_{2-x}S$ based on the UPS and DRS results (vs. NHE).

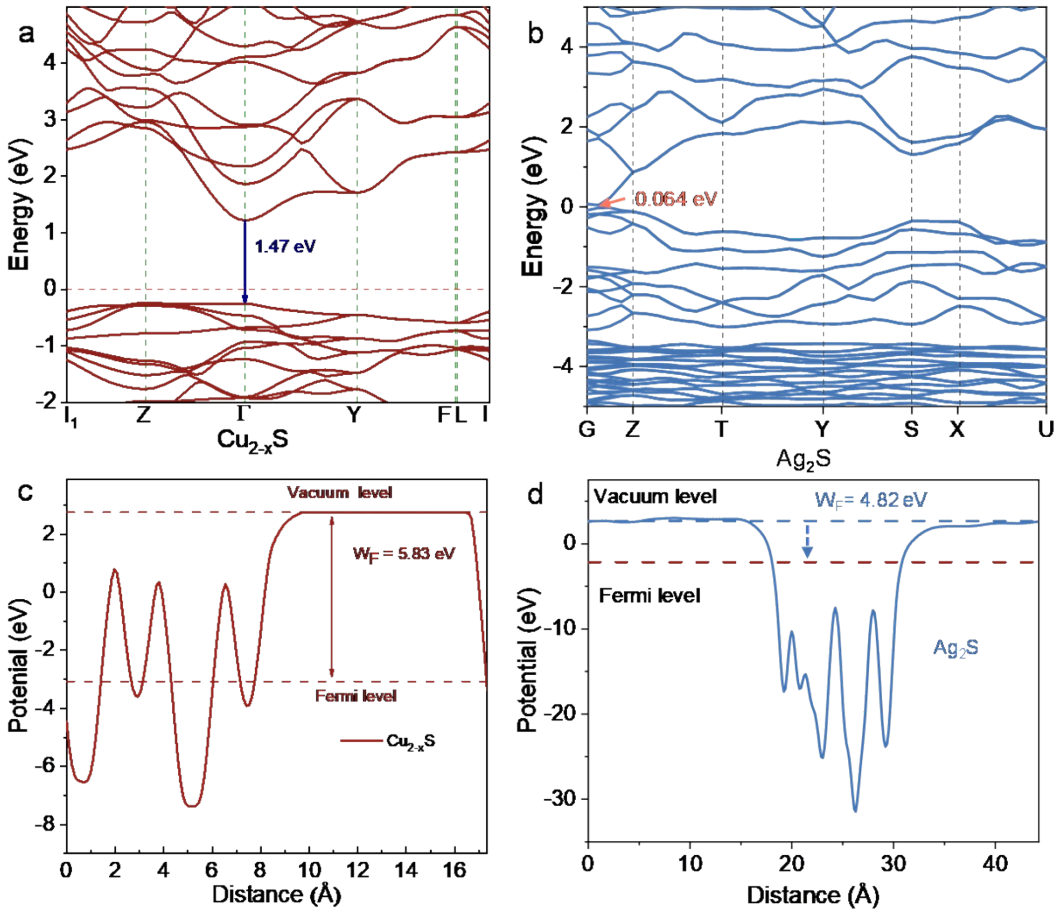

Figure S7. Calculated band structures (a, b) and Fermi levels (c, d) via DFT for Ag_2S and $Cu_{2-x}S$.

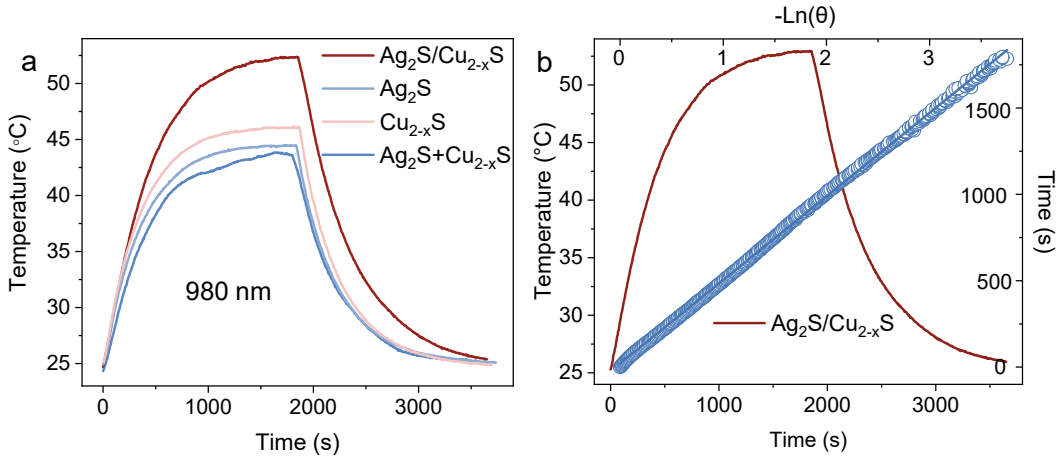

Figure S8. Photothermal heating curves for $Ag_2S/Cu_{2-x}S$ and components under a 980 nm laser (1.0 W/cm^2) irradiation. The time constant and PCE are calculated as 483.84 s and 48.57%, respectively.

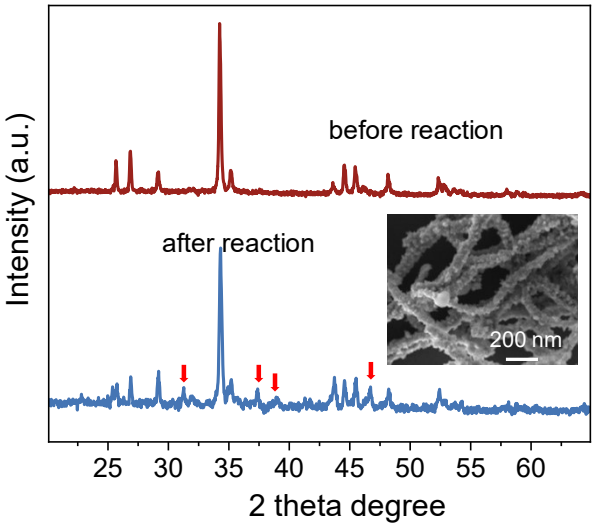

Figure S9. XRD patterns of $Ag_2S/Cu_{2-x}S$ nanotubes before and after reaction, the insert is the SEM image of $Ag_2S/Cu_{2-x}S$ nanotubes after reaction. The new peaks (labeled with red arrows) at 31.3 °, 37.4°, 38.9°, and 46.9° can be assigned to the (-112), (013), (-103), and (004) phases of Ag_2S.

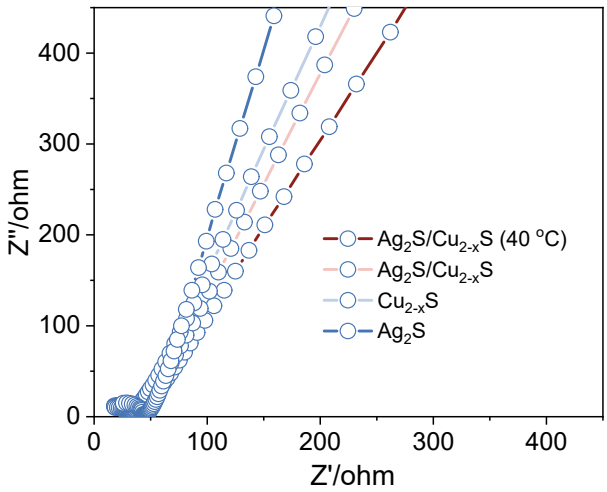

Figure S10. EIS plots of $Ag_2S/Cu_{2-x}S$ and components tested at 5 and 40 °C.

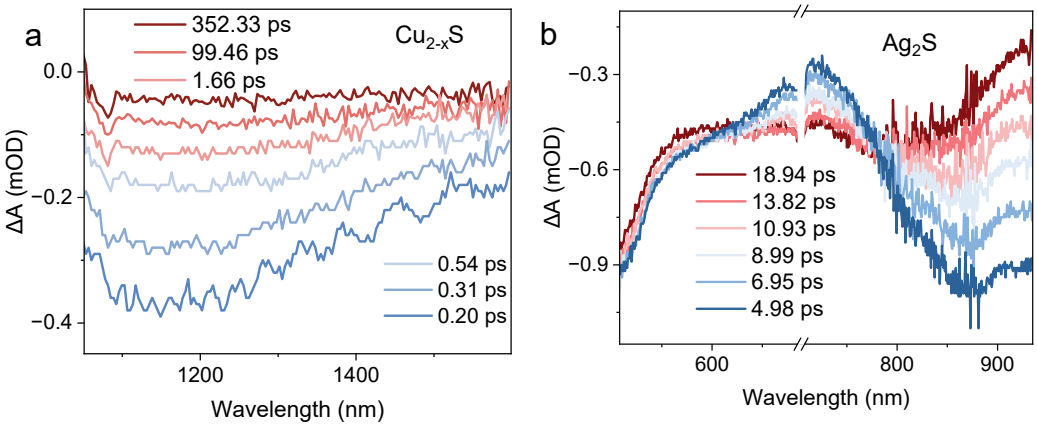

Figure S11. TA spectra of $Cu_{2-x}S$ (a) in the region of 1050-1640 nm) and Ag_2S (b) in the region of 500-900 nm.

Table S1. Comparison of the photothermal conversion performance of defective $Ag_2S/Cu_{2-x}S$ with similar materials.

Materials	PCE (%)	Reference
$Ag_2S/Cu_{2-x}S$	48.6	This work
Ag_2S NPs	38.5	(1)
$Ag-Ag_2S$	34.1	(2)
BSA-Ag_2S	18.9	(3)
Ag_2S@MSN-TGF	38.2	(4)
$Cu_xS–Ag_2S$	48.6	(5)
Ag_{2-x}/Cu_xS	44.0	(6)
$Ag_2S@WS_2$	33.0	(7)
$Fe_3O_4@Cu_{2-x}S$	34.1	(8)
$Cu_{2-x}S/CdS/Bi_2S_3$	31.0	(9)
$Cu_{2-x}S$-PEG@HA	30.5	(10)

References

[1] S. Zhu, W. Song, Y. He, Y. Wang, X. Li, Y. Wu, X. Meng, C. Lin, W. Wang, H. Wang, S. Huang, *ACS Appl. Mater. Interfaces* 2025, 17, 37465.

[2] P. Zang, Y. Du, C. Yu, D. Yang, S. Gai, L. Feng, J. Lin, *Chem. Mater*. 2023, 35(18), 7770-7780.

[3] J. Zhao, Q. Zhang, W. Liu, G. Shan, X. Wang, *Colloid Surface. B*. 2022, 211, 112295.

[4] W. Li, S. Liu, S. Dong, S. Gai, F. Zhang, Y. Dong, D. Yang, F. He, L. Zhong, P. Yang, *Chem. Eng. J.* 2021, 405, 127027.

[5] P. Zang, C. Yu, R. Zhang, D. Yang, S. Gai, B. Liu, J. Lin, *Adv. Mater.* 2024, 36(24), 2400416.

[6] Y. Zhao, M. Song, X. Yang, J. Yang, C. Du, G. Wang, J. Yi, G. Shan, D. Li, L. Liu, D. Yan, *Chem. Eng. J.* 2020, 399, 125777.

[7] Y. Lin, D. Han, Y. Li, L. Tan, X. Liu, Z. Cui, X. Yang, Z. Li, Y. Liang, S. Zhu, S. Wu, *ACS Sustainable Chem. Eng.* 2019, 7, 14982.

[8] B. Wang, T. Peng, Z. Jiang, L. Shen, J. Dong, Z. Song, J. Qu, X. Dai, *Talanta*, 2025, 284, 127189.

[9] M. Guo, T. Zhao, Z. Xing, Y. Qiu, K. Pan, Z. Li, S. Yang, W. Zhou, *ACS Appl. Mater. Interfaces* 2020, 12, 40328.

[10] X. Gao, M. Wei, D. Ma, X. Yang, Y. Zhang, X. Zhou, L. Li, Y. Deng, W. Yang, *Adv. Funct. Mater.* 2021, 31, 2106700.